Supplementary Figures

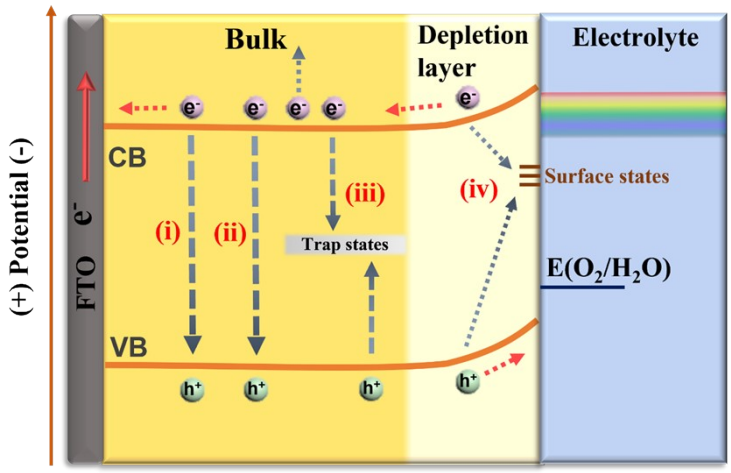

Fig. S1 Schematic illustration of various charge carrier recombination processes within an n-type semiconductor photoanode in contact with electrolyte, mainly including: (i) Direct radiative recombination (bimolecular decay), (ii) Auger band-to-band recombination, (iii) Shockley-Read-Hall (trap-assisted) recombination, and (iv) interface recombination processes through surface states.

Charge carrier recombination represents the reverse process of photoexcitation. Under thermodynamic equilibrium, the rates of charge carrier generation and recombination are equal. Depending on whether photon emission accompanies electron-hole recombination, recombination mechanisms are generally classified into radiative and nonradiative processes. As schematically shown in Fig. S1, radiative band-to-band recombination involves the spontaneous annihilation of free electrons and holes, accompanied by the emission of photons with energies close to the semiconductor bandgap. This process is particularly prominent in direct bandgap semiconductors. In contrast, nonradiative recombination pathways dissipate the recombination energy without photon emission and mainly include Auger recombination, Shockley-Read-Hall (SRH) recombination, and interface-related recombination. In Auger recombination, both energy and momentum conservation are satisfied through the excitation of a third charge carrier, which subsequently relaxes to the band edge via carrier–phonon interactions, converting the excess energy into lattice heat. Because the Auger recombination rate strongly depends on carrier concentration, this process becomes significant in highly doped or high-injection semiconductors, such as silicon. Radiative and Auger recombination are intrinsic processes governed by the fundamental electronic structure of the semiconductor and therefore define the theoretical upper limit of the charge carrier lifetime. In photoelectrochemical (PEC) systems, however, these intrinsic recombination pathways typically play a secondary role in determining device performance. More severe efficiency losses generally arise from extrinsic recombination channels associated with bulk defects, impurities, and surface or interfacial states, as exemplified by SRH and interface recombination. These defect-related states act as efficient recombination centers that impede bulk charge separation and suppress interfacial charge transfer, ultimately leading to degraded PEC performance.

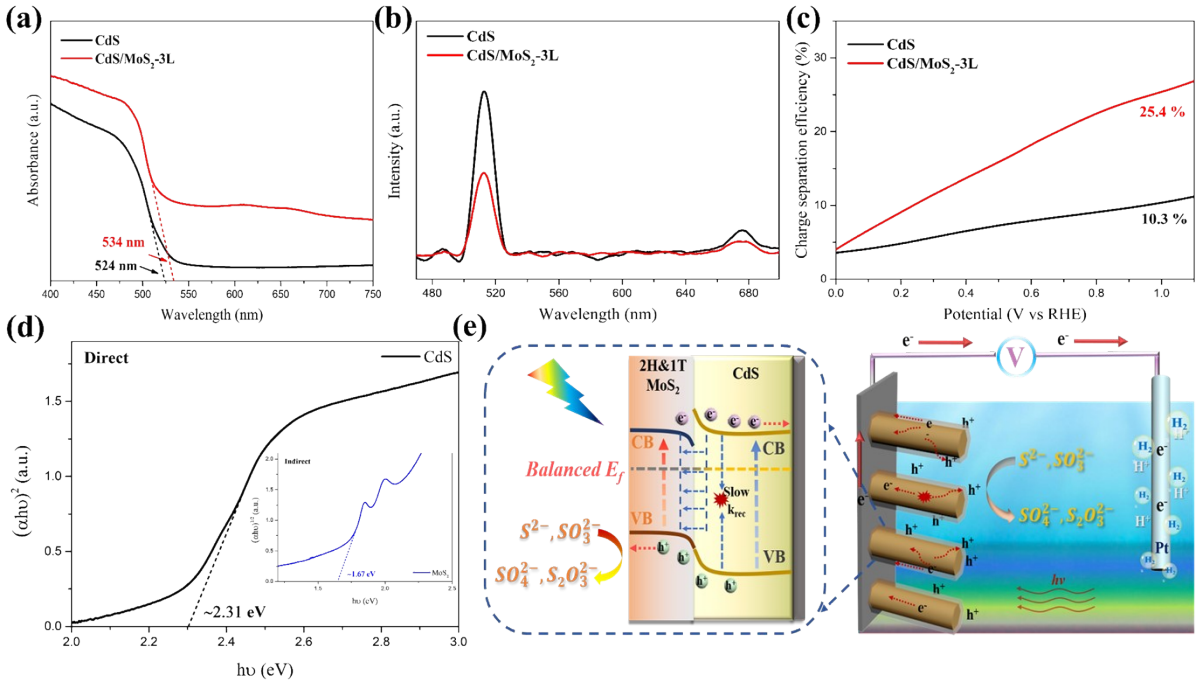

Fig. S2 (a) UV–vis-NIR diffuse reflectance spectroscopy (DRS) analysis, (b) photoluminescence (PL) tests, (c) the calculated charge separation efficiencies over the pristine CdS and CdS/MoS_2-3L heterojunction photoanode; (d) Tauc plots of the bare CdS and MoS_2 nanoflakes; (e) Schematic illustration of charge transfer models on the 1D/2D CdS/MoS_2 Type-I heterojunction photoanode system. Reprinted from Ref. 32 with permission. Copyright 2023 Elsevier.

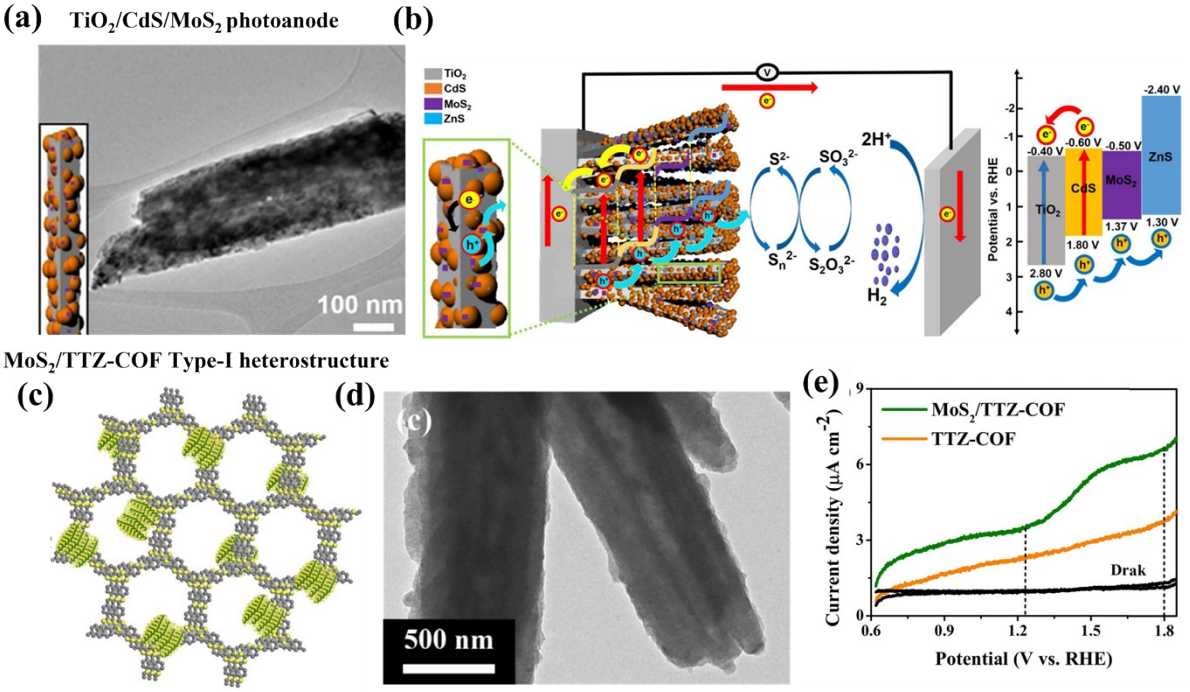

Fig. S3 (a) TEM image of TiO_2/CdS/MoS_2 film with the structural diagram as the insert; (b) The corresponding straddling/staggered energy band alignment and possible type II/type I charge transport pathway over the reported TiO_2/CdS/MoS_2 heterojunction photoanode. Reprinted from Ref. 78 with permission. Copyright 2019 Elsevier. (c) The structural diagram and (d) TEM image of the MoS_2/TTZ-COF nanocomposite; (e) LSV curves measured at 0.1 M Na_2SO_4 based on a three-electrode setup over the bare TTZ-COF and MoS_2/TTZ-COF Type I heterostructure photoanodes. Reprinted from Ref. 85. with permission. Copyright 2022 Elsevier.

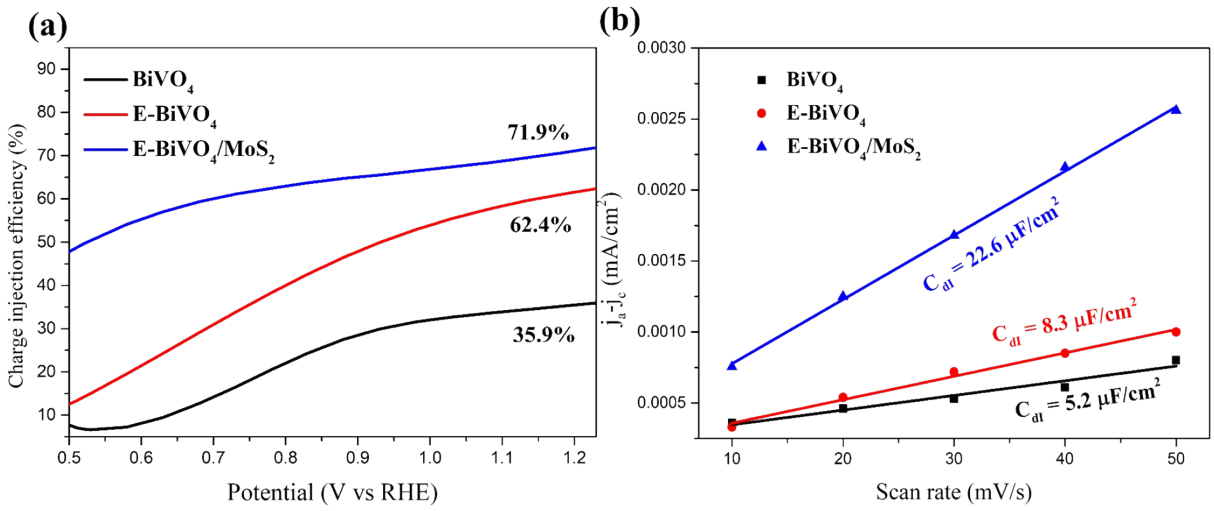

Fig. S4 (a) The calculated charge injection efficiency and (b) electrochemical surface-active areas (ECSA) analysis over the E-$BiVO_4$/MoS_2 Type-II heterojunction photoanode system. Reprinted from Ref. 77 with permission. Copyright 2023 Elsevier.

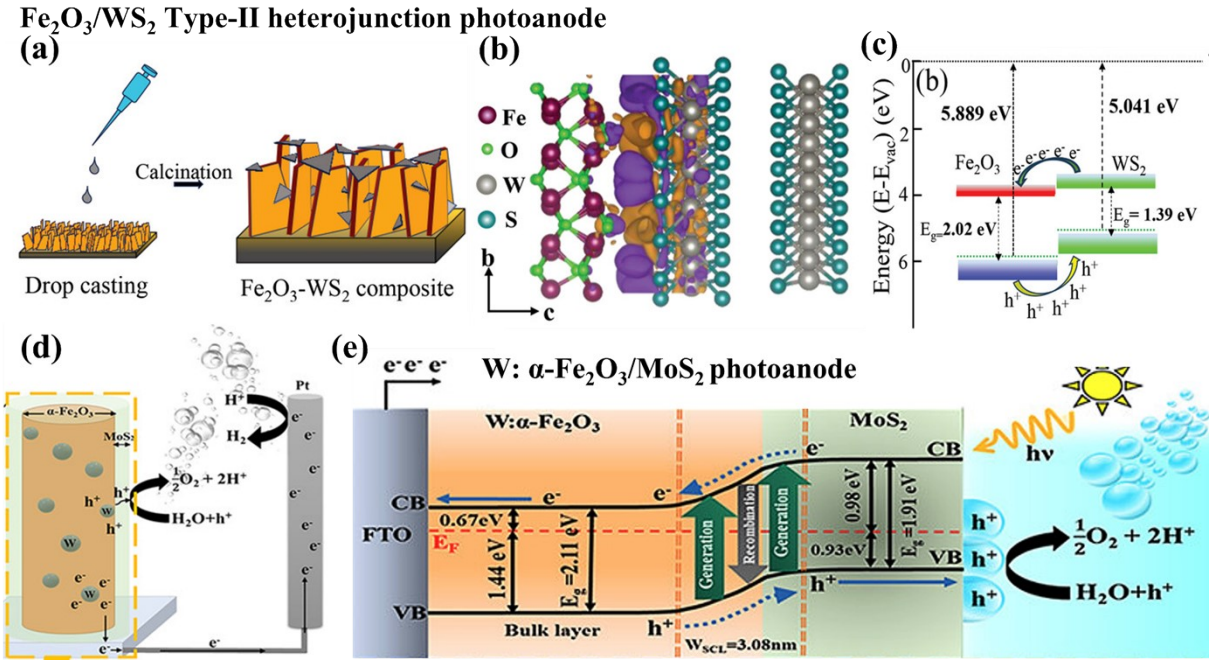

Fig. S5 (a) The synthetic route of the Fe_2O_3/WS_2 heterojunction photoanode; (b) Charge density difference of Fe_2O_3/WS_2 heterostructure. Charge accumulation and depletion are shown in the purple and dark orange regions at the interface; (c) Staggered energy band distribution and charge transfer pathways between Fe_2O_3 (110) and WS_2; Reproduced from Ref. 104. with permission. Copyright 2024 John Wiley and Sons. (d, e) Schematic illustration of the PEC water splitting reaction and the corresponding Type-II electron-hole separation and transport process over the reported W: α-Fe_2O_3/MoS_2 heterojunction photoanode. Reprinted from Ref. 86. with permission. Copyright 2021 American Chemical Society.

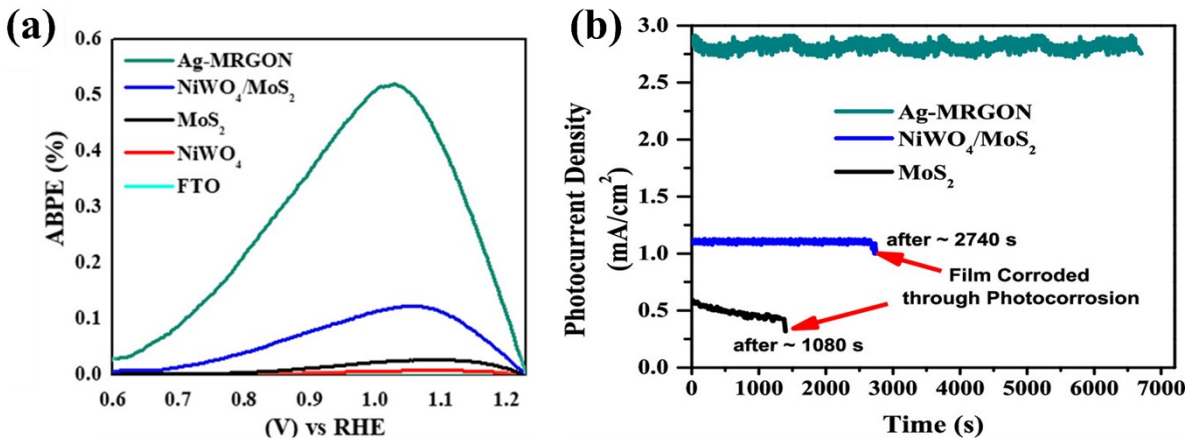

Fig. S6 (a) The calculated photoconversion efficiencies (% ABPE) vs potential of MoS_2 NSs, $NiWO_4$ NPs, $MoS_2/NiWO_4$, and Ag-MRGON heterojunction photoanodes; (b) Steady-state photocurrent densities as a function of time for MoS_2 NPs, $MoS_2/NiWO_4$ heterojunction, and Ag-MRGON all-solid-state Z-scheme heterojunction photoanodes measured at 1.0 V_{RHE}. Reprinted from Ref. 109 with permission. Copyright 2020 American Chemical Society.

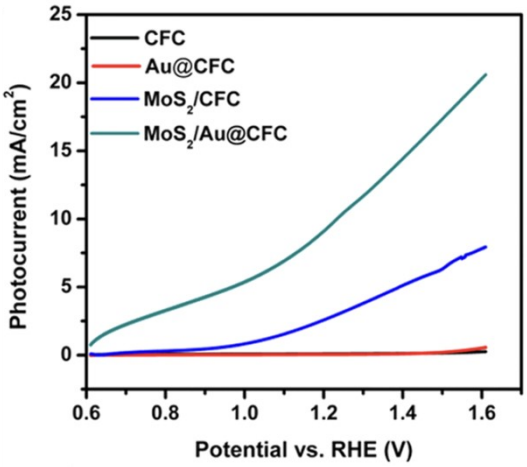

Fig. S7 LSV curves of CFC, Au@CFC, MoS_2/CFC, and MoS_2/Au@CFC Schottky junction photoanode systems. Reprinted from Ref. 119. with permission. Copyright 2017 American Chemical Society.

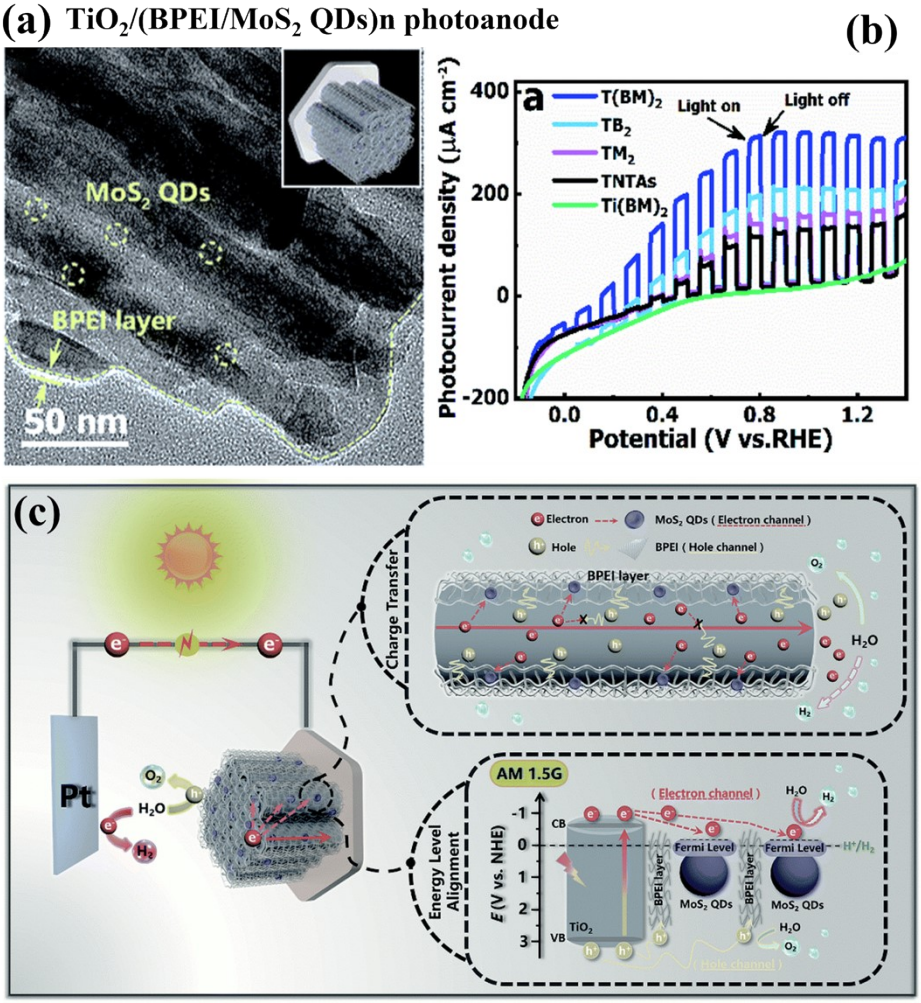

Fig. S8 (a) TEM image of TiO_2/(BPEI/MoS_2 QDs)$_2$ film; (b) Chopped LSV curves of $T(BM)_2$, TB_2, TM_2, TNTAs and $Ti(BM)_2$ measured in 0.5 M Na_2SO_4 under one sun illumination with a conventional three-electrode setup; (c) The plausible PEC water splitting mechanism over the reported TiO_2/(BPEI/MoS_2 QDs)n photoanode system. Reproduced from Ref. 120 with permission. Copyright 2020 Royal Society of Chemistry